Computationally Efficient Overmodulation Methods for Synchronous Motor Drive Systems

Qianwen Duan, Wei Tian, *Member, IEEE,* Qifan Yang, *Student Member, IEEE,* Xiaonan Gao, *Member, IEEE,* Yao Mao, *Member, IEEE,* Petros Karamanakos, *Senior Member, IEEE,* Ralph Kennel, *Senior Member, IEEE,* and Marcelo Lobo Heldwein, *Senior Member, IEEE*

***Abstract*—This paper presents two computationally efficient methods for selecting the optimal modulated voltage that can achieve superior dynamic performance for surface-mounted permanent magnet synchronous motors (SPMSMs). Specifically, when an SPMSM suffers a large reference or sudden load change, the controller might command a voltage reference which is beyond the range of voltages that a modulator can synthesize. In such cases, the transient behavior of the motor can deteriorate when the demanded voltage is not properly limited to the voltage boundary. To address this issue, a simple overmodulation method based on common-mode-saturation injection (CMSI) is proposed. This strategy comes with very low computational cost and can easily find the voltage vector on the boundary which is nearest to the reference voltage vector. Moreover, an alternative control method, referred to as quadratic program (QP) based deadbeat (DB) control, is proposed that also ensures optimal system performance during overmodualtion. According to this strategy, the control problem is formulated as a constrained QP, which is solved with an efficient solver based on an active-set method. Finally, extensive simulative and experimental investigations for an SPMSM are presented to demonstrate the effectiveness of the proposed overmodulation methods.**

***Index Terms*—Overmodulation, quadratic programming, model predictive control, surface-mounted permanent magnet synchronous motors (SPMSMs).**

I. Introduction

SURFACE-MOUNTED permanent magnet synchronous motors (SPMSMs) are used in many different areas such as aerospace [1], textile industry [2], industrial robots [3], vehicular transportation systems [4], etc., due to their high power density and fast dynamic torque response. The most widely adopted control method for SPMSMs is field-oriented control (FOC) [5]. In FOC, since proportional-integral (PI) controllers cannot handle the system physical constraints, some saturation methods are usually implemented to limit the voltage reference within the linear modulation region of carrier-based pulse width modulation (CB-PWM) or within the extended linear modulation region of space vector modulation (SVM) which are depicted in Fig. 1 [6], [7].

Manuscript received March 30, 2022; revised July 12, 2022 and August 12, 2022; accepted September 13, 2022. This work was supported in part by China Scholarship Council under Grant numbers CSC202004910658, and in part by the Deutsche Forschungsgemeinschaft (DFG, German Research Foundation) under Project 432509817 and 418870390. (Corresponding author: Wei Tian)

Q. Duan and Y. Mao are with Key Laboratory of Optical Engineering, Chinese Academy of Sciences, 610209 Chengdu, China; Institute of Optics and Electronics, Chinese Academy of Sciences, 610209 Chengdu, China; University of Chinese Academy of Sciences, 100049 Beijing, China; e-mail: duanqianwen16@mails.ucas.ac.cn, maoyao@ioe.ac.cn

W. Tian, Q. Yang, X. Gao, R. Kennel, and M. Heldwein are with the Chair of High-Power Converter Systems, Technical University of Munich, 80333 Munich, Germany; e-mail: wei.tian@tum.de, qifan.yang@tum.de, xiaonan.gao@tum.de, marcelo.heldwein@tum.de, ralph.kennel@tum.de

P. Karamanakos is with the Faculty of Information Technology and Communication Sciences, Tampere University, 33101 Tampere, Finland; e-mail: p.karamanakos@ieee.org

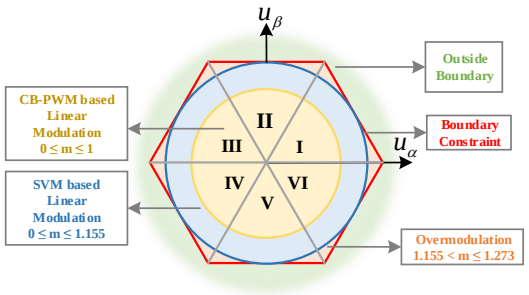

Fig. 1. Modulation regions for modulation voltage index in stationary reference frame [7].

The overmodulation region is the area between the inscribed circle and the hexagon boundary which can further increase the utilization of the dc-link voltage when SPMSMs encounter a large reference or sudden load changes [8]. Hence, in the last decades, some effective methods have been proposed to exploit the overmodulation region for SPMSM drives with PI controllers. In [9], the space vector Fourier analysis is added to the voltages produced by SVM, while the converter is operating in the overmodulation region. Based on that, six-step operation, in which case the output voltage follows the hexagon boundary, is achieved by rotating the voltage reference and utilizing the so-called dynamic overmodulation technique [10]. However, despite the effectiveness of this overmodulation method, the limited control bandwidth of PI controllers still limits the dynamic performance of FOC.

Recently, some modern drive control algorithms for SPMSMs have attracted significant attention. Model predictive control (MPC) is one of the most extensively studied methods due to its ability to consider explicit constraints on, e.g., the input and state [11]. MPC can be classified into two categories, i.e., direct [12] and indirect MPC [13]. The most popular direct MPC method, known as finite control set MPC (FCS-MPC), directly computes the optimal switch positions by minimizing the error between the reference and predicted values of the controlled variables, e.g., the load current [14]. In [15], the voltage limit boundary is realized with a field-oriented rectangular boundary area to ensure six-step operation. Moreover, six-step operation based on a boundary constraint can be achieved by appropriately designing the cost function of the optimization problem [16]. FCS-MPC when not properly designed can lead to significant current and torque ripples that can have an adverse effect on the drive system [16].

Different from direct MPC, indirect MPC operates the power electronic systems at a fixed switching frequency and generates deterministic harmonic spectra owing to a dedicated modulation stage [17]. The optimal problem underlying direct MPC is normally formulated as a constrained quadratic pro-

gram (QP), which can account for the physical limitations of the system since these are implemented as explicit system constraints. However, the discrete nature of power electronics is neglected on a first stage, after which, a modulator needs to be implemented to complete the current control task [18].

To solve the QP problem underlying indirect MPC, different solution methods can be adopted. For example, an active-set algorithm is implement to solve the MPC-based QP in a computationally efficient manner [19]. In [20], a method based on neural networks is employed to find the optimal solution of the QP problem. But the high complexity and heavy computational burden of this algorithm make such a method impractical.

As an alternative, deadbeat (DB) control can be used instead. Such a control method can be considered as a simplified version of indirect MPC, namely when a one-step prediction horizon is used and no constraints are designed. The reference voltage computed by the DB controller is in essence the unconstrained solution of the equivalent indirect MPC problem. Therefore, when the reference voltage is beyond the voltage boundary, a proper saturation method has to be adopted to find a feasible solution on the boundary constraint. This means that the unconstrained DB solution needs to be appropriately handled such that it will respect the physical limitations of the system. For instance, in [21], the unconstrained solution is saturated to the circle inscribed in the space vector hexagon. This, however, leads to a slow transient behavior, since the dc-link voltage is not fully used. A second method is to solve the constrained DB problem, which is formulated as a constrained QP, to ensure that the voltage reference is within the voltage boundary [22]. However, the method in [22] is not experimentally verified due to the challenge of solving constrained QP problems in real-time. Moreover, these two overmodulation methods, i.e., DB solution with overmodulation methods and the constrained DB solution have not been sufficiently compared on a theoretical level to investigate their relationship.

In the view of the above, the novelty and contribution of this paper are summarized in the following.

1) An unconstrained DB controller is designed to solve the current control problem. Subsequently, a computationally efficient overmodulation method based on common-mode-saturation injection (CMSI) is proposed to limit the output voltage.
2) A QP-based DB overmodulation method is presented that employs a computationally efficient active-set QP solver. Thanks to this, the constrained DB method is implemented on a real-time platform and is experimentally tested.
3) A comprehensive performance assessment is provided based on both simulations and experiments. The presented results show that the two proposed overmodulation methods achieve exactly the same control performance. Furthermore, to show the global equivalence between the two methods, a mathematical proof is also provided.

The rest of this paper is organized as follows. In Section II, we present the mathematical model and model predictive current control of the SPMSM system. The two overmodulation methods are proposed in Section III. In Section IV, we validate the two presented methods with simulation and experiments. The comparisons with the state-of-art overmodulation methods are also shown in detail. The discussion in Section V provides insight into the applicability and relevant applications of the two proposed methods. Finally, the summary is given in Section VI.

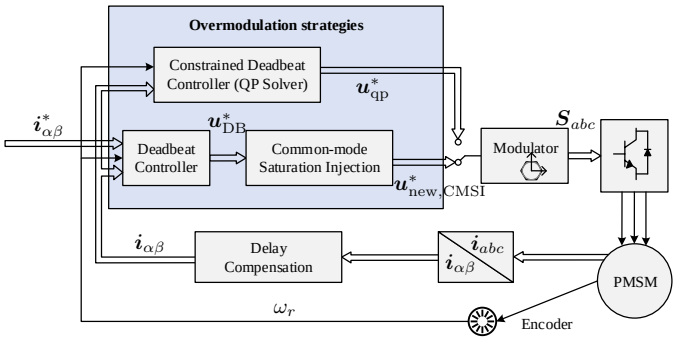

Fig. 2. Proposed current control structure suitable for overmodulation.

II. System Modelling and Current Control

The structure of the discussed current control structure for an SPMSM driven by a two-level voltage source inverter is shown in Fig. 2. In this section, the system dynamic modelling and framework of the current controller will be first introduced.

A. SPMSM Drive Model

The dynamic model of an SPMSM in the stationary reference frame $\alpha\beta$ is

$$\frac{\mathrm{d}\boldsymbol{i}_{s,\alpha\beta}}{\mathrm{d}t} = -\frac{R_s}{L_s}\boldsymbol{i}_{s,\alpha\beta} + \frac{1}{L_s}\boldsymbol{v}_{\alpha\beta} + \psi_f\omega_r \begin{bmatrix} \sin\phi_r \\ -\cos\phi_r \end{bmatrix}, \quad (1)$$

where $\boldsymbol{i}_{s,\alpha\beta} = \begin{bmatrix} i_{s\alpha} & i_{s\beta} \end{bmatrix}^T$ denotes the stator current, and $\boldsymbol{v}_{\alpha\beta} = \begin{bmatrix} v_\alpha & v_\beta \end{bmatrix}^T$ the stator voltage. $R_s, L_s, \psi_f, \omega_r$ and ϕ_r are the stator resistance, stator inductance, permanent magnet flux, electrical rotor speed, and electrical rotor position, respectively. Define $\boldsymbol{u}_{abc} = \begin{bmatrix} u_a & u_b & u_c \end{bmatrix}^T$ as the three-phase input signal of the modulator where $u_x \in [-1, 1]$ with $x \in \{a, b, c\}$. The modulating signal $\boldsymbol{u}_{abc}$ is transformed to $\boldsymbol{u}_{\alpha\beta}$ in the stationary reference frame through the Clarke transformation matrix

$$\boldsymbol{K} = \frac{2}{3}\begin{bmatrix} 1 & -\frac{1}{2} & -\frac{1}{2} \\ 0 & \frac{\sqrt{3}}{2} & -\frac{\sqrt{3}}{2} \end{bmatrix}. \quad (2)$$

Then the relation between the three-phase modulating signal $\boldsymbol{u}_{abc}$ and $\boldsymbol{v}_{\alpha\beta}$ is

$$\boldsymbol{v}_{\alpha\beta} = \frac{v_{\mathrm{dc}}}{2}\boldsymbol{u}_{\alpha\beta} = \frac{v_{\mathrm{dc}}}{2}\boldsymbol{K}\boldsymbol{u}_{abc}, \quad (3)$$

where v_{dc} is the dc-link voltage and $\boldsymbol{u}_{\alpha\beta}$ is the modulating signal in the stationary frame.

With (1), we can get the general state space model.[1]

$$\begin{aligned} \frac{\mathrm{d}\boldsymbol{x}(t)}{\mathrm{d}t} &= \boldsymbol{F}\boldsymbol{x}(t) + \boldsymbol{G}\boldsymbol{u}(t) + \boldsymbol{W}(t) \\ \boldsymbol{y}(t) &= \boldsymbol{C}\boldsymbol{x}(t) \end{aligned} \quad (4)$$

where $\boldsymbol{F}$ is the system matrix, $\boldsymbol{G}$ is the input matrix , and $\boldsymbol{C}$ is the output matrix, with

$$\begin{aligned} &\boldsymbol{F} = \begin{bmatrix} -\frac{R_s}{L_s} & 0 \\ 0 & -\frac{R_s}{L_s} \end{bmatrix}, \boldsymbol{G} = \frac{v_{\mathrm{dc}}}{2}\begin{bmatrix} \frac{1}{L_s} & 0 \\ 0 & \frac{1}{L_s} \end{bmatrix}, \\ &\boldsymbol{W} = \frac{\psi_f\omega_r}{L_s}\begin{bmatrix} \sin\phi_r \\ -\cos\phi_r \end{bmatrix}, \boldsymbol{C} = \begin{bmatrix} 1 & 0 \\ 0 & 1 \end{bmatrix}. \end{aligned} \quad (5)$$

[1]To simplify the notation, the subscript $\alpha\beta$ for vectors in the $\alpha\beta$-plane is omitted, while vectors in the abc-plane are denoted with the corresponding subscript.

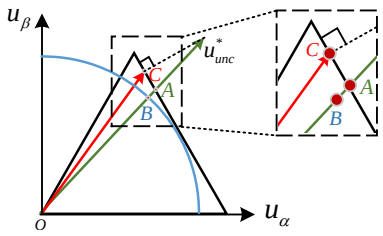

Fig. 3. The modulating signal which is not constrained.

By using forward Euler discretization, the discrete-time state-space model of the system is of the form

$$\begin{aligned} \boldsymbol{x}(k+1) &= \boldsymbol{A}\boldsymbol{x}(k) + \boldsymbol{B}\boldsymbol{u}(k) + \boldsymbol{D}(k) \\ \boldsymbol{y}(k) &= \boldsymbol{C}\boldsymbol{x}(k) \end{aligned}, \tag{6}$$

with $\boldsymbol{A} = \boldsymbol{I} + \boldsymbol{F}T_s$, $\boldsymbol{B} = \boldsymbol{G}T_s$, $\boldsymbol{D} = \boldsymbol{W}T_s$, where T_s is the sampling interval and $\boldsymbol{I}$ the identity matrix. It is worth noting that (6) is sufficiently accurate only when ϕ_r slowly varies within T_s.

B. Current Control Problem

The system model (6) enables the prediction of the current at step $k+1$, i.e., $\boldsymbol{i}_s(k+1)$, for a given control input $\boldsymbol{u}(k)$. For the conventional DB method, we have

$$\boldsymbol{y}(k+1) = \boldsymbol{C}\left[\boldsymbol{A}\boldsymbol{x}(k) + \boldsymbol{B}\boldsymbol{u}(k) + \boldsymbol{D}(k)\right]. \tag{7}$$

Let $\boldsymbol{y}^*(k+1)$ denote the current reference at step $k+1$. Then the control input can be obtained as

$$\boldsymbol{u}^*_{\mathrm{DB}}(k) = (\boldsymbol{C}\boldsymbol{B})^{-1}\left[\boldsymbol{y}^*(k+1) - \boldsymbol{C}\boldsymbol{A}\boldsymbol{x}(k) - \boldsymbol{C}\boldsymbol{D}\right]. \tag{8}$$

It is worth noting that the modulating signal $\boldsymbol{u}^*_{\mathrm{DB}}$ in (8) is not constrained, and it is easy to go beyond the boundary constraint of the voltage hexagon during transients. Let $\boldsymbol{u}^*_{\mathrm{unc}} = \boldsymbol{u}^*_{\mathrm{DB}}$ denote the unconstrained modulating signal in the $\alpha\beta$ reference frame. The region outside the boundary constraint is not accessible, hence a feasible modulating signal needs to be found.

For the sake of illustration, we assume that the modulating signal $\boldsymbol{u}^*_{\mathrm{unc}}$ locates in sector I as shown in Fig. 3. Traditionally, $\boldsymbol{u}^*_{\mathrm{unc}}$ is limited to the SVM linear modulation region (inscribed circle (INC) in the hexagon), which is depicted as $\overrightarrow{OB}$ in Fig. 3 [21]. Due to the low utilization of the dc-link voltage, this saturation method leads to sluggish response during transients. An alternative way of redefining the modulating signal is the direct constraint process which limits $\boldsymbol{u}^*_{\mathrm{unc}}$ to the boundary ($\overrightarrow{OA}$ in Fig. 3) [23]. However even if this method fully utilizes the available voltage and has a faster response than $\overrightarrow{OB}$, it is still not optimal. The reason is that the terminal point of the vector $\overrightarrow{OC}$ has the smallest distance from the terminal point of the modulating signal $\boldsymbol{u}^*_{\mathrm{unc}}$. Therefore, using $\overrightarrow{OC}$ allows for the minimum reference current tracking error. For this reason, an effective method to compute this modulating signal is required. By subsequently driving this modulating signal to the modulator the transient performance of SPMSM drives will be improved.

III. Overmodulation Methods

In this section, we discuss four overmodulation methods. First, the overmodulation methods introduced in [24] and [25] are presented, which use a geometrical approach to obtain the constrained modulating signal reference. Following, the proposed method of CMSI is investigated, which is significantly simpler to implement and yields exactly the same results as the method in [24] and [25]. Finally, the constrained DB method based on an active-set QP solver is also presented to highlight the optimality of the proposed overmodulation methods.

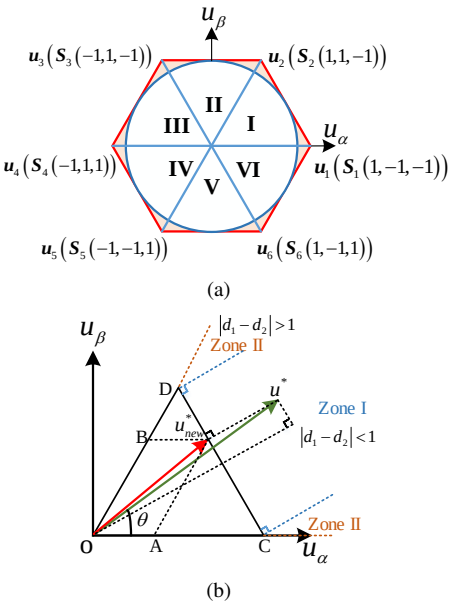

Fig. 4. (**a**) Six sectors in stationary reference frame. (**b**) The SVM overmodulation method when the modulating signal is outside the boundary constraint.

A. Overmodulation Method for SVM

For SVM, the stationary reference frame is divided into six sectors according to the six modulating signals which correspond to the six three-phase switch positions, shown in Fig. 4(a). The phase of the modulating signal $\boldsymbol{u}^*$ determines to which sector it belongs. Take sector I for example. The two adjacent active voltage vectors $(\boldsymbol{u}_1, \boldsymbol{u}_2)$ from sector I and the zero-voltage vector $(\boldsymbol{u}_0)$ synthesize $\boldsymbol{u}^*(k)$

$$\boldsymbol{u}^*(k) = \boldsymbol{u}_1 d_1 + \boldsymbol{u}_2 d_2 + \boldsymbol{u}_0 d_0, \tag{9}$$

with the duty cycles d_1, d_2, d_0, and the relation is $d_1 + d_2 + d_0 = 1$. When $\boldsymbol{u}^*$ is within the boundary constraint, the duty cycles for $\boldsymbol{u}_1$ and $\boldsymbol{u}_2$ are

$$\begin{aligned} d_1 &= \tfrac{2}{\sqrt{3}}\tfrac{|\boldsymbol{u}^*|}{|\boldsymbol{u}_1|}\sin\left(\tfrac{\pi}{3} - \theta\right) \\ d_2 &= \tfrac{2}{\sqrt{3}}\tfrac{|\boldsymbol{u}^*|}{|\boldsymbol{u}_2|}\sin(\theta) \end{aligned}, \tag{10}$$

where θ is the phase of $\boldsymbol{u}^*$ in the stationary reference frame.

The area beyond the boundary constraint is divided into two zones based on the value of $|d_1 - d_2|$ calculated based on (10), i.e. Zone I and Zone II illustrated in Fig. 4(b). When the condition $|d_1 - d_2| < 1$ is true, the feasible reference signal $\boldsymbol{u}^*_{\mathrm{new,SVM}}$ needs to be decided by orthogonal projection of $\boldsymbol{u}^*$ on the boundary constraint. To synthesize this new reference $\boldsymbol{u}^*_{\mathrm{new,SVM}}$, the duty cycles of d'_1 and d'_2 that correspond to $\boldsymbol{u}_1$ and $\boldsymbol{u}_2$, respectively, need to be calculated. These should satisfy

$$\boldsymbol{u}^*_{\mathrm{new,SVM}} = \boldsymbol{u}_1 d'_1 + \boldsymbol{u}_2 d'_2. \tag{11}$$

According to the equilateral triangle in Fig. 4(b) for $\theta \in \left(0, \tfrac{\pi}{3}\right]$, these are

$$\begin{aligned} d'_1 &= \tfrac{1}{2} - \tfrac{3}{4}|\boldsymbol{u}^*|\sin\left(\theta - \tfrac{\pi}{6}\right) \\ d'_2 &= \tfrac{1}{2} + \tfrac{3}{4}|\boldsymbol{u}^*|\sin\left(\theta - \tfrac{\pi}{6}\right) \end{aligned}. \tag{12}$$

On the other hand, when the condition $|d_1 - d_2| > 1$ holds, which means $\boldsymbol{u}^*$ is in Zone II, only the active vector adjacent to $\boldsymbol{u}^*$ is used [24]. Finally, the same procedure is followed for the other sectors, thus it is not repeated here.

With the above, the SVM overmodulation method proposed in [24] is completely described.

B. Overmodulation Method with Modulated Model Predictive Control

Modulated model predictive control (M2PC) is a recently proposed MPC scheme, which can also achieve optimal performance in the overmodulation zone [25]. Instead of calculating the unconstrained optimal modulating signal $\boldsymbol{u}^*_{\text{unc}}$, M2PC calculates the predicted stator current $\boldsymbol{i}_s(k+1)$ for each voltage vectors $\boldsymbol{u}_i$, with $i \in \{0, 1, ...7\}$, for the next time step, i.e.,

$$\boldsymbol{i}_{s,i}(k+1) = \boldsymbol{A}\boldsymbol{i}_s(k) + \boldsymbol{B}\boldsymbol{u}_i(k) + \boldsymbol{D}(k). \tag{13}$$

Then, the predicted tracking error $\boldsymbol{e}_i = \boldsymbol{i}^*_s(k+1) - \boldsymbol{i}_{s,i}(k+1)$ for each of the voltage vectors is evaluated, and the two active voltage vectors that result in the smallest $||\boldsymbol{e}_i||^2_2$ are selected to synthesize the modulating signal.

As an illustrative example, consider the reference current $\boldsymbol{i}^*_s$ in Fig. 5(a) that lies in the overmodulation region. The two predicted currents that are closest to the reference current are the vectors $\boldsymbol{i}_{s,1}$ and $\boldsymbol{i}_{s,2}$. Thus, the modulating signal $\boldsymbol{u}^*_{\text{M2PC}}$ is synthesized by the two active voltage vectors $\boldsymbol{u}_1$ and $\boldsymbol{u}_2$ according to

$$\boldsymbol{u}^*_{\text{M2PC}} = d_1\boldsymbol{u}_1 + d_2\boldsymbol{u}_2\,, \tag{14}$$

with $d_1 + d_2 = 1$ and $d_1, d_2 \geq 0$.

From Fig. 5(a), it is evident that the minimum reference tracking error is achieved with $\boldsymbol{i}_{\text{M2PC}}$, where $(\boldsymbol{i}_{\text{M2PC}} - \boldsymbol{i}^*_s) \perp (\boldsymbol{i}_{s,1} - \boldsymbol{i}_{s,2})$. By applying elementary geometry in Fig. 5(a), it is straightforward to show that the duty cycles d_1 and d_2 are given by

$$d_1 = \frac{||\boldsymbol{e}_1||\cos(\beta)}{||\boldsymbol{e}_3||}, \tag{15a}$$

$$d_2 = \frac{||\boldsymbol{e}_2||\cos(\alpha)}{||\boldsymbol{e}_3||}\,, \tag{15b}$$

with

$$\cos(\alpha) = \frac{\boldsymbol{e}_1^T \cdot \boldsymbol{e}_3}{||\boldsymbol{e}_1||\,||\boldsymbol{e}_3||}\,, \quad \cos(\beta) = \frac{\boldsymbol{e}_2^T \cdot (-\boldsymbol{e}_3)}{||\boldsymbol{e}_2||\,||\boldsymbol{e}_3||}\,, \tag{16a}$$

$$\boldsymbol{e}_1 = \boldsymbol{i}^*_s - \boldsymbol{i}_{s,1}\,, \quad \boldsymbol{e}_2 = \boldsymbol{i}^*_s - \boldsymbol{i}_{s,2}\,, \quad \boldsymbol{e}_3 = \boldsymbol{i}_{s,2} - \boldsymbol{i}_{s,1}\,. \tag{16b}$$

Finally, it is worth mentioning that if one of the calculated α and β is larger than $\frac{\pi}{2}$, which corresponds to the case shown in Fig. 5(b), the active voltage vector that results in the smallest $||\boldsymbol{e}_i||^2$ is applied for the whole sampling interval, i.e., $d_2 = 1$ and $d_1 = 0$ in Fig. 5(b).

C. Overmodulation Method based on Common-Mode-Saturation Injection

An alternative to SVM, CB-PWM is more convenient for implementation. And it is known that the traditional CB-PWM with a min/max common-mode voltage injection is equivalent to SVM [26]. After the injection process, it is a common practice to saturate the (instantaneous) three-phase modulating signal $u_x \in [-1, 1]$ with $x \in \{a, b, c\}$. However, in previous studies, the operations that combined injection with saturation were not analyzed in detail. It will be proved in the following that the proposed CMSI method, which is an overmodulation

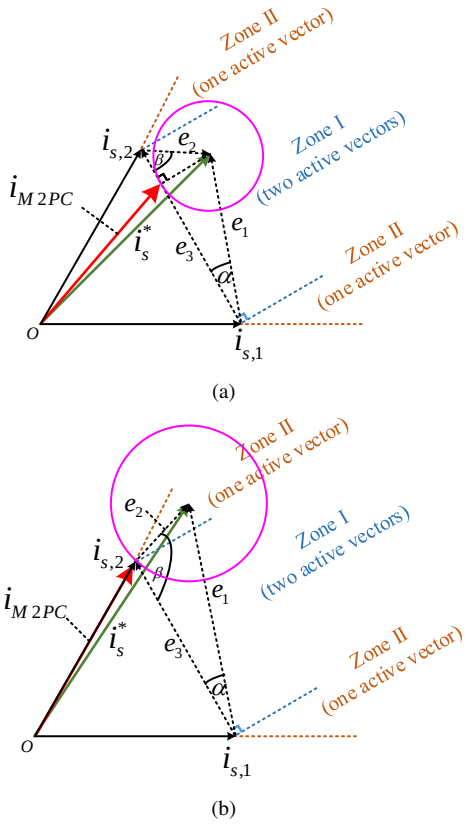

Fig. 5. Geometrical analysis of the overmodulation zone. (**a**) Overmodulation with two active vectors. (**b**) Overmodulation with one active vector.

strategy that combines common-mode voltage injection and saturation, is equivalent to the method in Section III-A.

Concretely, the min/max common-mode voltage

$$u_0 = -\frac{1}{2}\left[\min\left(\boldsymbol{u}^*_{\text{unc}}\right) + \max\left(\boldsymbol{u}^*_{\text{unc}}\right)\right], \tag{17}$$

is chosen as the injection signal. Then the modulating signal becomes,

$$\boldsymbol{u}_{abc,\text{com}} = \boldsymbol{u}^*_{\text{unc}} + u_0. \tag{18}$$

Finally, the new reference $\boldsymbol{u}^*_{\text{new,CMSI}}$ is defined as

$$\boldsymbol{u}^*_{\text{new,CMSI}} = \boldsymbol{K}\,\text{sat}\left(\boldsymbol{u}_{abc,\text{com}}\right), \tag{19}$$

where $\text{sat}\left(\boldsymbol{u}_{abc,\text{com}}\right) = \min\left(\max\left(\boldsymbol{u}_{abc,\text{com}}, -1\right), 1\right)$.

Remark 1: The modulating signal $\boldsymbol{u}^*_{\text{new,SVM}}$ calculated by SVM and $\boldsymbol{u}^*_{\text{new,CMSI}}$ deduced from the CMSI overmodulation method, are completely equivalent, as shown in Appendix A. This implies that the transient performance should be the same regardless of the overmodulation method adopted. However, it is worth pointing out that the CMSI method proposed in this paper is less computationally intensive and simpler to implement as shown in Section IV.

D. QP Solver based Constrained DB Method

Different from the geometrical solution, a constrained DB method is proposed in this section that allows for a computationally efficient solver. The basic principle is to select the optimal modulating signal which minimizes the cost function that describes the output current error between its reference and its predicted value. Thus, the cost function is defined as

$$\begin{aligned} J\left(\boldsymbol{x}\left(k\right), \boldsymbol{u}\left(k\right)\right) &= \left\|\boldsymbol{y}\left(k+1\right) - \boldsymbol{y}^*\left(k+1\right)\right\|^2 \\ &= \left\|\boldsymbol{M}\boldsymbol{u}\left(k\right) + \boldsymbol{r}\right\|^2, \end{aligned} \tag{20}$$

where $\boldsymbol{M} = \boldsymbol{C}\boldsymbol{B}$, and $\boldsymbol{r} = \boldsymbol{C}\boldsymbol{A}\boldsymbol{x}\left(k\right) + \boldsymbol{C}\boldsymbol{D} - \boldsymbol{y}^*\left(k+1\right)$.

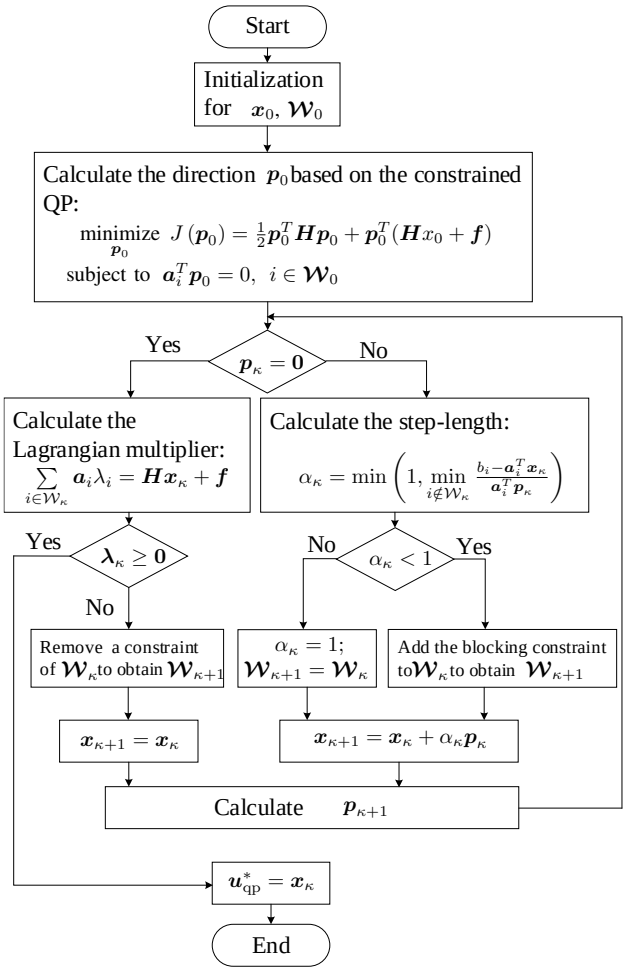

Fig. 6. The algorithm of the implemented primal active-set method.

After some algebraic manipulations and by dropping the constant term, the following QP problem is formulated

$$\begin{array}{ll}\underset{\boldsymbol{u}(k)\in\mathbb{R}^2}{\text{minimize}} & J = \frac{1}{2}\boldsymbol{u}^T\boldsymbol{H}\boldsymbol{u} + \boldsymbol{u}^T\boldsymbol{f} \\ \text{subject to} & \boldsymbol{a}_i^T\boldsymbol{u} \geq b_i,\ i \in \mathcal{I}\end{array}, \tag{21}$$

where $\boldsymbol{H} = 2\boldsymbol{M}^T\boldsymbol{M}$ is a symmetric and positive definite matrix, i.e., the Hessian matrix, $\boldsymbol{f} = 2\boldsymbol{M}^T\boldsymbol{r}$, and $\mathcal{I} = \{1, 2, ..., 6\}$ corresponds to the hexagon boundary constraint,

$$[\boldsymbol{a}_1\ \boldsymbol{a}_2\ \boldsymbol{a}_3\ \boldsymbol{a}_4\ \boldsymbol{a}_5\ \boldsymbol{a}_6] = \begin{bmatrix} -\sqrt{3} & 0 & \sqrt{3} & \sqrt{3} & 0 & -\sqrt{3} \\ -1 & -1 & -1 & 1 & 1 & 1 \end{bmatrix}, \tag{22a}$$

$$[b_1\ b_2\ b_3\ b_4\ b_5\ b_6] = -\begin{bmatrix} \frac{4}{\sqrt{3}} & \frac{2}{\sqrt{3}} & \frac{4}{\sqrt{3}} & \frac{4}{\sqrt{3}} & \frac{2}{\sqrt{3}} & \frac{4}{\sqrt{3}} \end{bmatrix}. \tag{22b}$$

As the solving time of the QP problem (21) is a significant factor for real-time implementation, a primal active-set method (PASM) is employed due to its high efficiency and reliability. It generates solutions in an iterative manner that remain in the feasible region with respect to the primal problem (21) while steadily decreasing the value of the cost function [27]. Based on the PASM, the inequality-constrained problem (21) is transformed into the equality-constrained problem, which is summarized in the flowchart shown in Fig. 6. To clearly understand it, the following definitions are required.

Definition 1: (Active set) At any feasible $\boldsymbol{u}$, the active set $\mathcal{A}(\boldsymbol{u})$ consists of indices of the inequality constraints i for which $\boldsymbol{a}_i^T\boldsymbol{u} = b_i$, i.e.,

$$\mathcal{A}(\boldsymbol{u}) = \left\{i \in \mathcal{I} \,\middle|\, \boldsymbol{a}_i^T\boldsymbol{u} = b_i\right\}. \tag{23}$$

Then, the inequality constraint $i \in \mathcal{I}$ is said to be active if $\boldsymbol{a}_i^T\boldsymbol{u} = b_i$ and inactive if $\boldsymbol{a}_i^T\boldsymbol{u} > b_i$.

Definition 2: (Working set) At the iteration κ, the working set consists of the indices in which the inequality constraints are imposed as equality constraints, and it is denoted as $\boldsymbol{\mathcal{W}}_\kappa$.

To elucidate the solution process visualized in Fig. 6, let $\boldsymbol{x}_\kappa$ denote $\boldsymbol{u}_{\mathrm{qp},\kappa}$ in Fig. 6, which is the optimal solution of (21) at iteration κ. First, a feasible starting point $\boldsymbol{x}_0$ and a working set $\boldsymbol{\mathcal{W}}_0$ need to be determined. Then, $\boldsymbol{x}_\kappa$ is updated at each iteration with $\boldsymbol{x}_{\kappa+1} = \boldsymbol{x}_\kappa + \alpha_\kappa\boldsymbol{p}_\kappa$, in which α_κ is the step-length, and $\boldsymbol{p}_\kappa$ is the direction at which the cost function value J_κ decreases. The direction $\boldsymbol{p}_\kappa$ is computed by solving an equality-constraint QP subproblem, in which the constraints in $\boldsymbol{\mathcal{W}}_\kappa$ are imposed as equality constraints, while the remaining inequality constraints are temporarily ignored. As $\boldsymbol{a}_i^T(\boldsymbol{x}_\kappa + \boldsymbol{p}_\kappa) = b_i$, $i \in \boldsymbol{\mathcal{W}}_\kappa$, the QP subproblem that computes $\boldsymbol{p}_\kappa$ is

$$\begin{array}{ll}\underset{\boldsymbol{p}}{\text{minimize}} & J_{\mathrm{sub}}(\boldsymbol{p}_\kappa) = \frac{1}{2}\boldsymbol{p}_\kappa^T\boldsymbol{H}\boldsymbol{p}_\kappa + \boldsymbol{p}_\kappa^T\boldsymbol{f}' \\ \text{subject to} & \boldsymbol{a}_i^T\boldsymbol{p}_\kappa = 0,\ i \in \boldsymbol{\mathcal{W}}_\kappa\end{array}, \tag{24}$$

where $\boldsymbol{f}' = \boldsymbol{H}\boldsymbol{x}_\kappa + \boldsymbol{f}$. Then the solution of (24) can be easily found based on the techniques introduced in [27]. While solving this subproblem, the so-called Lagrangian multipliers $\boldsymbol{\lambda}_\kappa$ that correspond to each constraint are also obtained by

$$\sum_{i\in\mathcal{W}_k} \boldsymbol{a}_i\lambda_i = \boldsymbol{H}\boldsymbol{x}_k + \boldsymbol{f}. \tag{25}$$

If $\boldsymbol{p}_\kappa = \boldsymbol{0}$, there is no feasible direction at which J_κ can be decreased with the current working set $\boldsymbol{\mathcal{W}}_\kappa$. In such a case, the Lagrangian multipliers $\boldsymbol{\lambda}_\kappa$ need to be checked. If $\boldsymbol{\lambda}_\kappa \geq \boldsymbol{0}$ holds for all the constraints in the working set, then the optimal solution is found and the algorithm terminates. Otherwise, the constraint whose Lagrangian multiplier is negative should be removed from the working set $\boldsymbol{\mathcal{W}}_{\kappa+1}$ in the next iteration.

On the other hand, if $\boldsymbol{p}_\kappa \neq \boldsymbol{0}$, then the step-length α_κ is calculated as

$$\alpha_\kappa = \min\left(1, \min_{i\notin\boldsymbol{\mathcal{W}}_\kappa, \boldsymbol{a}_i^T\boldsymbol{p}_\kappa<0} \frac{b_i - \boldsymbol{a}_i^T\boldsymbol{x}_\kappa}{\boldsymbol{a}_i^T\boldsymbol{p}_\kappa}\right). \tag{26}$$

When $\alpha_\kappa < 1$, it means that the hexagon bound has been reached, and the $\boldsymbol{x}_\kappa$ is in the overmodulation region, i.e., on the hexagon boundary. Therefore, as shown in Fig. 6, a constraint is added to the working set $\boldsymbol{\mathcal{W}}_\kappa$, and in the next iteration the algorithm searches the solution only along the voltage hexagon boundary. Following, $\boldsymbol{x}_{\kappa+1} = \boldsymbol{x}_\kappa + \alpha_\kappa\boldsymbol{p}_\kappa$ is used for the next iteration, and the working set $\boldsymbol{\mathcal{W}}_{\kappa+1}$ is updated if $\boldsymbol{x}_{\kappa+1}$ activates a constraint that is not included in $\boldsymbol{\mathcal{W}}_\kappa$. To better understand the above concept, Appendix B provides two examples that elucidate the workings of the QP solver in question.

IV. Performance Assessment

In this section, we demonstrate the application of these four methods in an SPMSM drive system. The test bench is shown in Fig. 7. It consists of a dSPACE SCALEXIO real-time control system, interface, an SPMSM and an induction machine (IM) coupled together, an oscilloscope, a two-level inverter for the controlled machine (i.e., SPMSM), and an inverter for the load machine (i.e., IM). The parameters of the SPMSM drive are listed in Table I. Finally, because asymmetric sampling is used, the system sampling frequency and switching frequency are 20 kHz and 10 kHz, respectively.

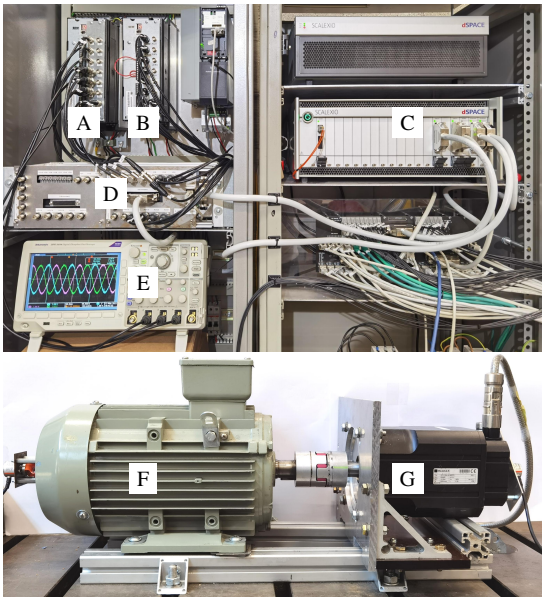

Fig. 7. Setup of the electrical drives testbench. A: Inverter for IM. B: Inverter for SPMSM. C: dSPACE SCALEXIO real-time control system. D: Interface. E: Oscilloscope. F: IM. G: SPMSM.

TABLE I
THE PARAMETERS OF THE SPMSM DRIVE.

Symbol	Quantity	Value
v_{dc}	Rated dc-link voltage	560 V
V_R	Rated voltage	380 V
I_R	Rated current	6.3 A
P_R	Rated power	2.76 KW
f_R	Rated stator frequency	150 Hz
N_R	Rated speed	3000 rpm
p	Pole pairs	3
R_s	Stator resistance	0.95 Ω
L_s	Synchronous inductance	0.95 mH

A. Simulation Studies at High Current

To clearly examine the current dynamics, the motor speed is controlled by the load motor so that only the current control loop is implemented for the SPMSM. The performance of the four overmodulation methods during a step of the current reference i_q^* from 0 to 1 per unit (p.u.) is shown in Fig. 8, which depicts the $\boldsymbol{i}_{dq}$ current tracking, phase current and the duty cycle performance. As can be seen in that figure, the performance of the four overmodulation techniques is identical. For example, the same current overshoot is observed in all four cases, while the phase current trajectories are identical. Finally, the derived duty cycles demonstrate the same behavior.

B. Experimental Results at High Current

To verify the equivalence of the four overmodulation techniques in an experimental setting, the same scenario as before is examined and the results are presented in Fig. 9. It can be seen that all these four methods have good current tracking as shown in the dq reference frame. The settling time is within 0.6ms. Nevertheless, the phase currents and duty cycles in the abc reference frame have some minute differences in transient and steady state. These are due to the non-idealities encountered in a real-world setup that do not allow an exact replication of the experimental conditions. Despite this, it can be observed that the behavior of the four overmodulation methods is very similar, as expected according to the theoretical analysis provided in Section III.

For further insight, the modulating signals (outside and inside hexagon) produced by the CMSI, SVM and QP-based DB methods are shown in Fig. 10. The direction of the arrows in Fig. 10 indicates the trajectory that the modulating signals follow in time. The points indicated as empty boxes are the unconstrained solutions solved by DB in (8), while the points shown as crosses are calculated by the CMSI, SVM, and QP-based DB methods. According to the conducted experiment, there are 12 voltage points outside the hexagon, which explain the settling time of 0.6 ms shown in Fig. 9. As for the M2PC method, a behavior similar to that of the other three aforementioned methods is observed. To further compare the modulating signals, the solutions computed by the four overmodulation methods are shown in Fig. 11(a). This figure again highlights the equivalence between the four methods.

As a commonly used overmodulation method is that of INC, i.e., limiting the modulating signal to the circle inscribed to the voltage hexagon,[2] it is necessary to compare the performance of the CMSI, SVM, QP-based DB, M2PC, and INC methods. Because of the consistency in the methods of CMSI, SVM, QP-based DB and M2PC, only one of them, i.e., the QP-based DB method, is selected for the subsequent demonstration. The comparisons between the QP-based DB and INC methods are shown in Fig. 11(b). The pink circles are the unconstrained solutions of QP-based DB, while the red boxes are those of INC. During the transition period, the numbers of discrete steps, in which the unconstrained modulating signals are outside the hexagon, are 12 and 16 for the QP-based DB and INC methods, respectively. This means that the QP-based DB method has a faster response than INC. More specifically, the settling times are 0.53ms and 0.8ms for the QP-based DB and INC methods, respectively, see Fig. 12. This is an improvement by 50.9% compared to the INC method.

For the drive systems, a key variable for evaluating the behavior of the four discussed overmodulation methods is the total harmonic distortion (THD) of the output current. The spectra in Fig. 13 show that the harmonics of i_a generated by the CMSI, SVM, QP-based DB, and M2PC methods appear at similar frequencies—mostly at the sidebands of the switching frequency of 10 kHz—and are of comparable amplitude. The current THD values for the CMSI, SVM, QP-based DB, and M2PC methods are 4.6302%, 4.2996%, 4.4257%, and 4.2812%, respectively. This implies that the steady-state performance of these four overmodulation methods is very similar as there is a very close match on the produced current harmonic energy.

C. Experimental Results with Insufficient DC-Link Voltage

An advantage of overmodulation is the utilization of the dc-link voltage to the maximum extent, which maximizes the line-to-line voltage at the motor terminals. Therefore, an experimental test with insufficient dc-link voltage is also performed. In this scenario, the dc-link voltage is reduced to 70% of its rated value, and the current tracking results are shown in Fig. 14. It can be observed that the INC method in Fig. 14(d) has a significant steady-state tracking error. In contrast, the tracking performance of the CMSI, SVM, QP-based DB and M2PC overmodulation methods is clearly

[2]This is equal to the method mentioned in [21].

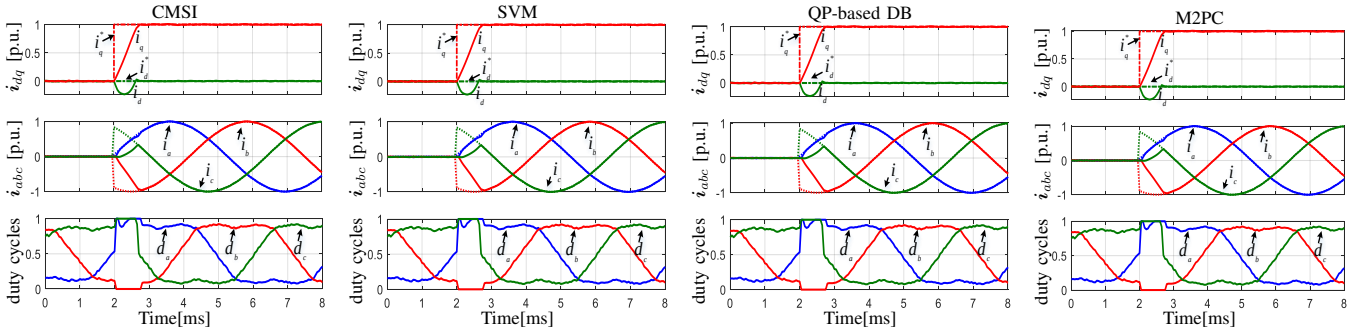

Fig. 8. Simulation results of current reference tracking with four overmodulation methods in the per unit system.

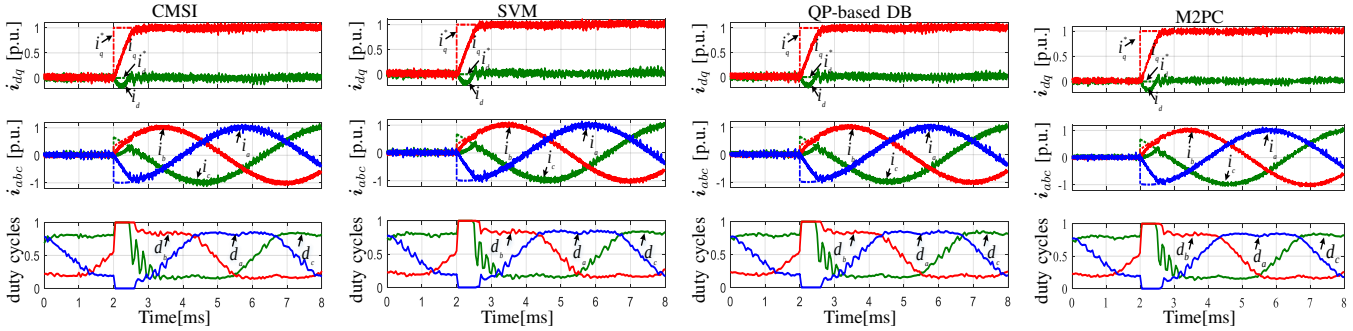

Fig. 9. Experimental results of current reference tracking with four overmodulation control methods in the per unit system.

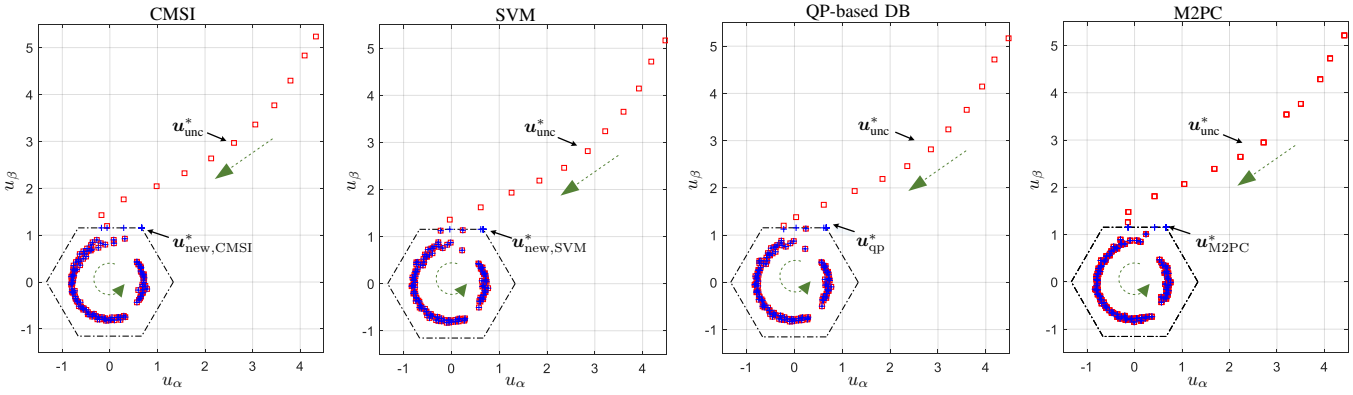

Fig. 10. The modulating voltage computed by four overmodulation methods.

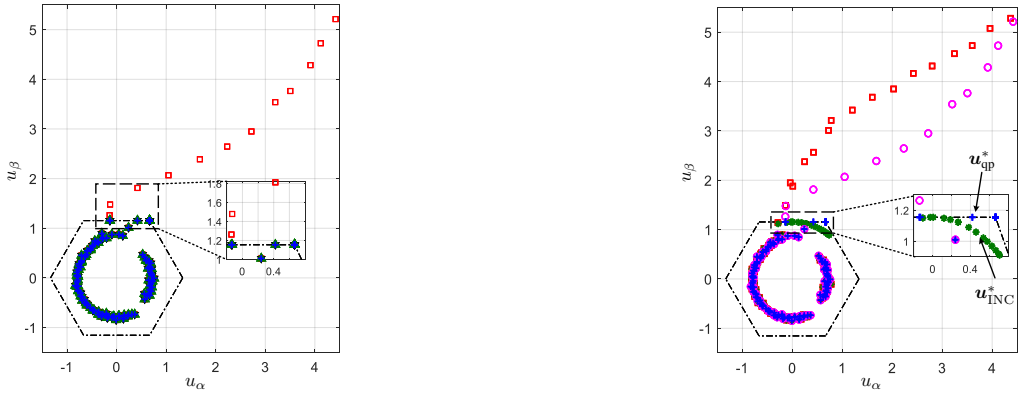

Fig. 11. (a) The four overmodulation methods of SVM, M2PC, CMSI and QP-based DB are equivalent. (b) The modulating voltage computed by the QP-based DB and INC methods. The pink circles are the unconstrained solutions of QP-based DB, while the red boxes are those of INC.

better both in transient and steady state. Nevertheless, it is worth mentioning that the transient duty cycles in Fig. 14(b) are somewhat different from these in Figs. 14(a), 14(c) and 14(e) due to the non-ideal setup of the experimental platform. Finally, the corresponding modulating signals are shown in Fig. 15, to provide more insight into the tracking performance shown in Fig. 14.

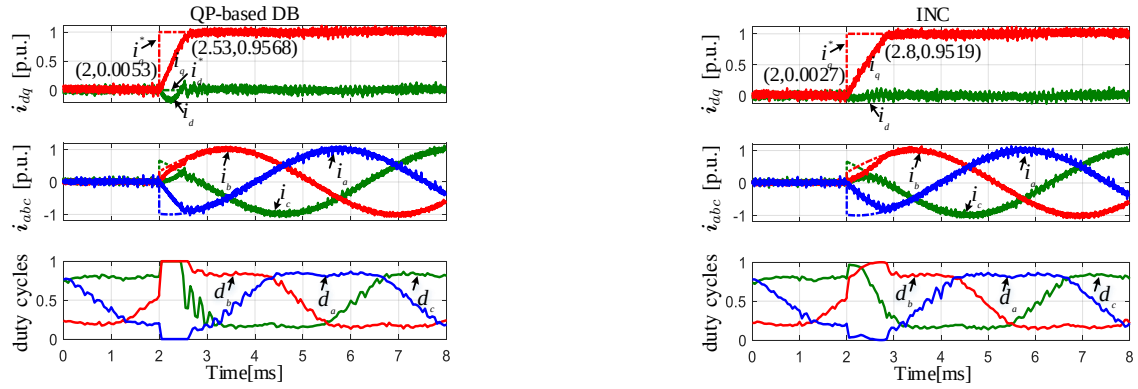

Fig. 12. The comparisons between the QP-based DB and INC methods for current tracking.

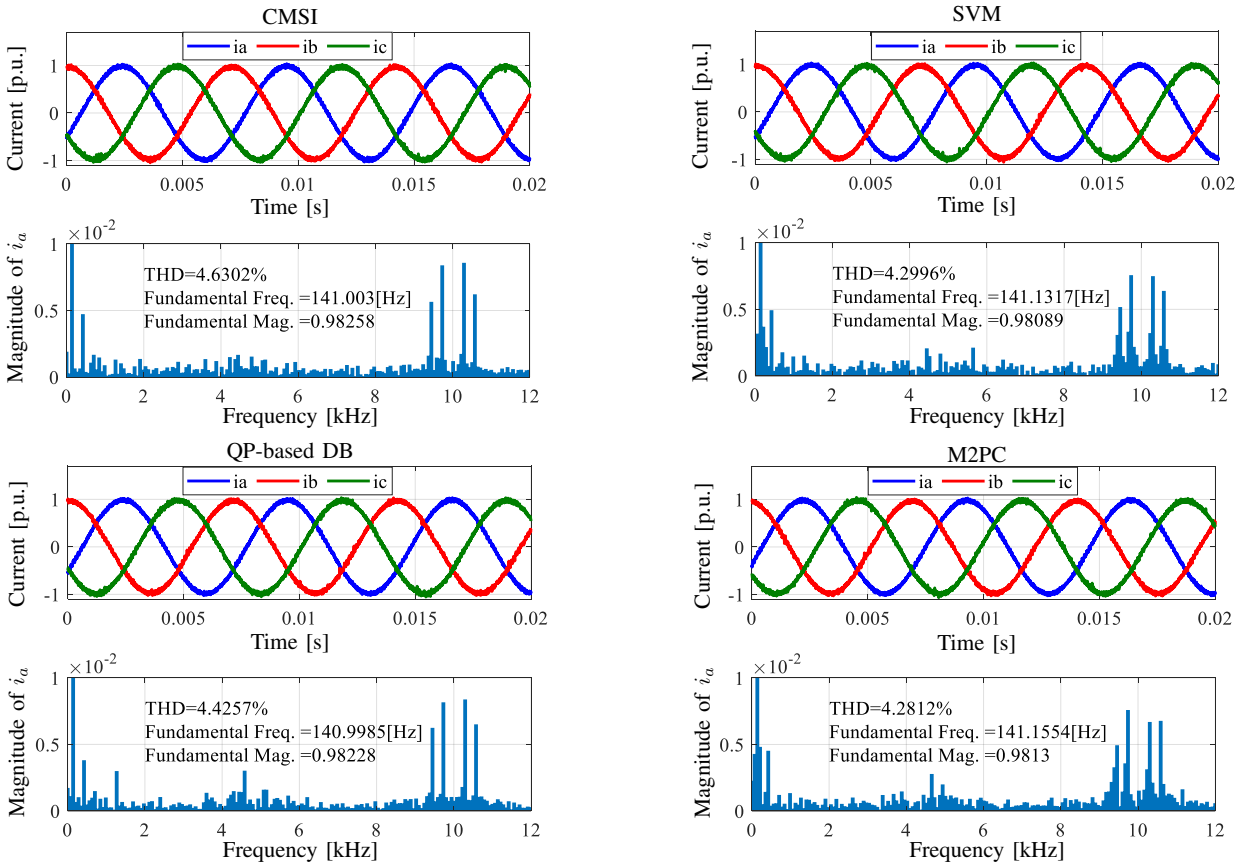

Fig. 13. The harmonic distortion analysis of the output current for the CMSI, SVM, QP-based DB, and M2PC methods.

D. Experimental Results under Changes in the DC-Link Voltage

As demonstrated in the previous sections, the current response of the INC method is slower than that of the proposed methods due to the limited voltage margin, as this is limited to the linear modulation region. To further investigate this, the response of the INC method and the proposed overmodulation techniques to changes in the dc-link voltage is examined in this section. Because of the similar behavior of CMSI and QP-based DB, the CMSI method is selected for demonstration purposes in Fig. 16. As can be seen in Fig. 16(b), when the dc-link voltage drops to 60% of its nominal value, a significant current tracking error instantly appears due to the inability of the INC method to provide sufficient voltage. On the other hand, when the CMSI overmodulation method is adopted, a favorable behavior is observed, see Fig. 16(a). Specifically, as can be seen, the controller manages to successfully track the current reference, even when the dc-link voltage sharply decreases. This, however, comes at a cost of an increased ripple on the q-component of the current due to the operation on the hexagon bound.

TABLE II
COMPARISON OF COMPUTATIONAL TIMES

Method		CMSI	SVM	QP-based DB	INC	M2PC
Time (μs)	Maximum	7.3	8.5	10.4	7.6	11.8
	Average	6.5	7.8	8.3	6.4	10.2

E. Analysis of the Computational Burden

Since the main computational burden relates to the computation time, the turnaround time on dSPACE is analyzed. Table II summarizes the maximum and average times of the five discussed control algorithms, i.e., CMSI, SVM, QP-based DB,

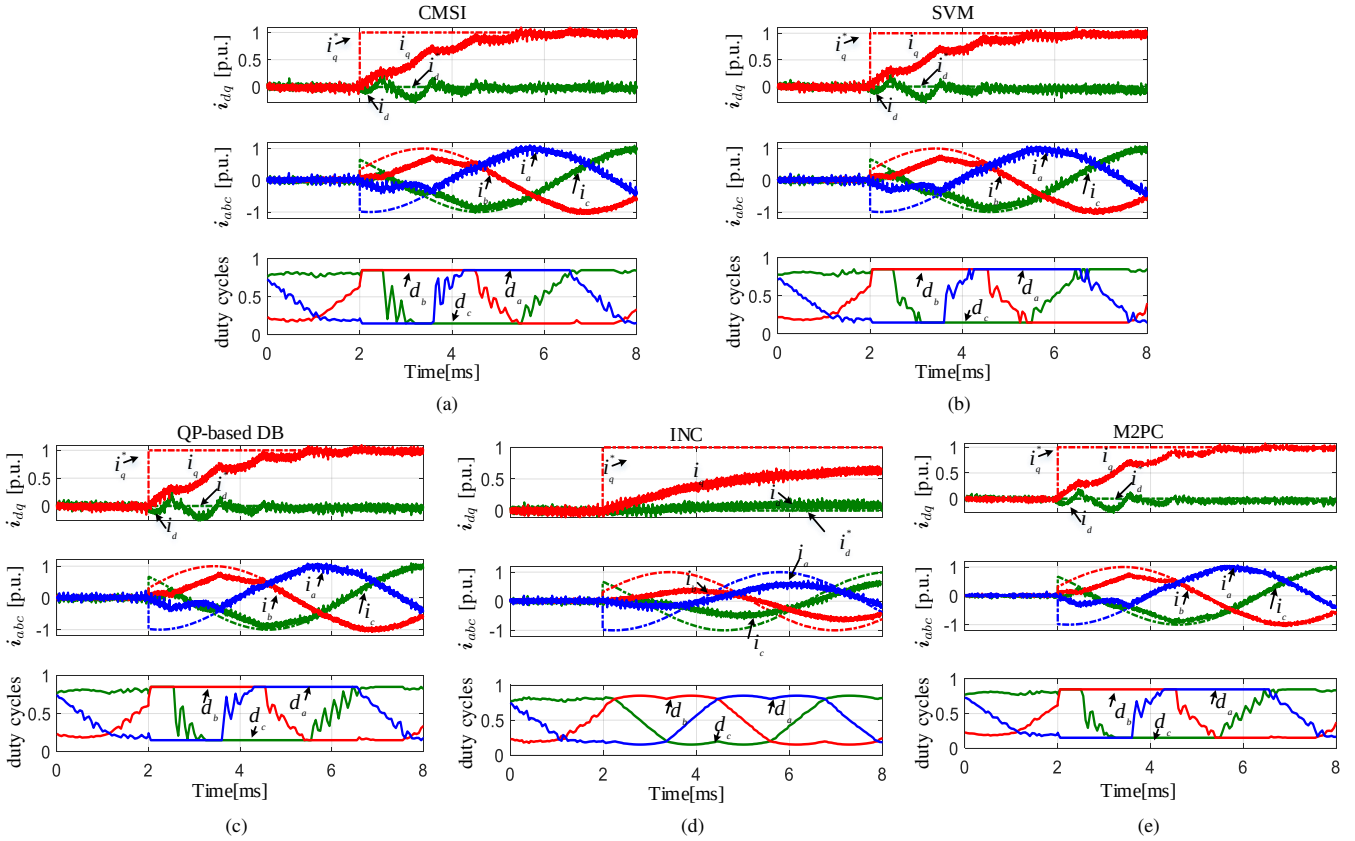

Fig. 14. Experimental results for current reference tracking with five overmodulation control methods when the dc-link voltage is 70% of its rated value (results in p.u.).

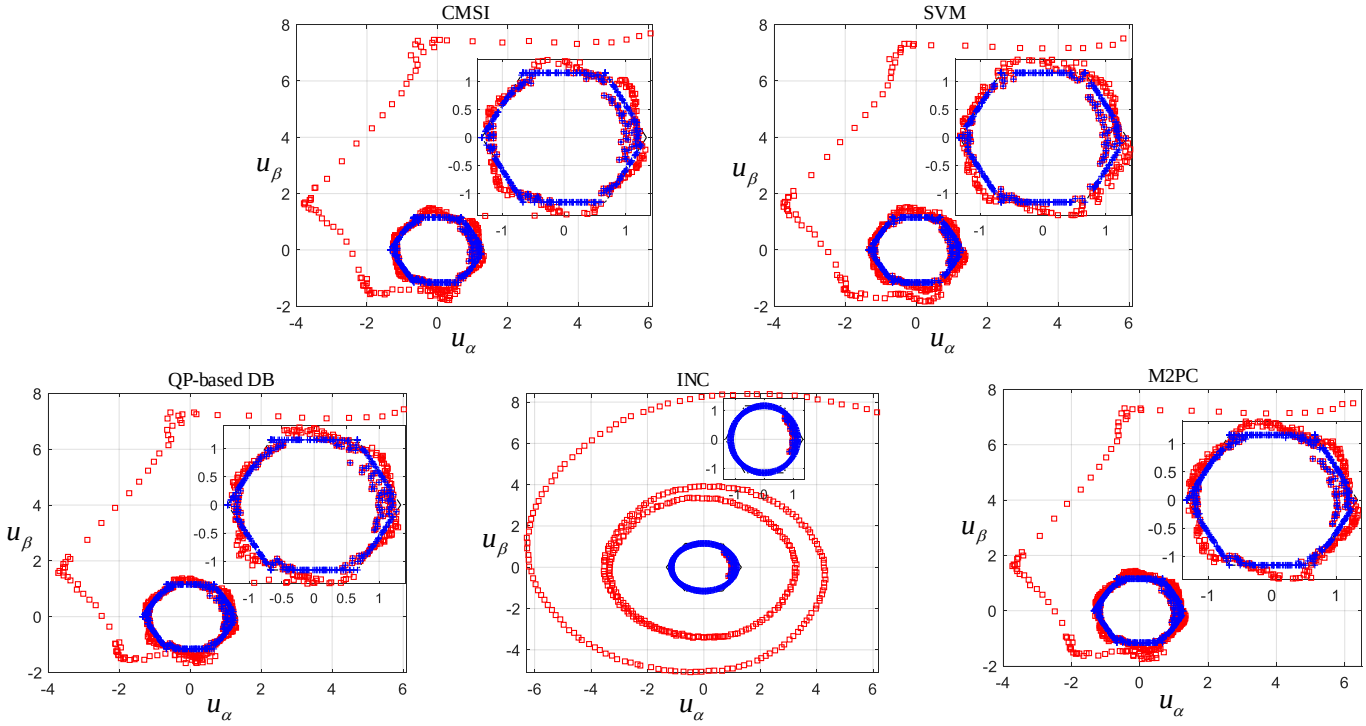

Fig. 15. The modulating voltage computed by five overmodulation methods.

M2PC and INC. As can be seen, the CMSI and INC methods demonstrate similar computation times. Hence, it is clear that the CMSI method is the most effective method owing to the adopted algorithm presented in Section III-C. On the other hand, the biggest turnaround time among these five methods is that of M2PC. This is due to the procedure adopted to compute the desired duty cycles that requires the exhaustive evaluation of all possible voltage vectors, see Section III-B. The second biggest time is that of QP-based DB because of the QP solver. As for the SVM method, it needs to calculate the modulating signals that belong to six sections, so the average time is slightly bigger than that of CMSI. Hence, the overmodulation strategy of CMSI may be the preferable option for machines without anisotropy. On the other hand, a QP-based DB overmodulation approach may be better when the level sets are not circular. In such a case, the proposed

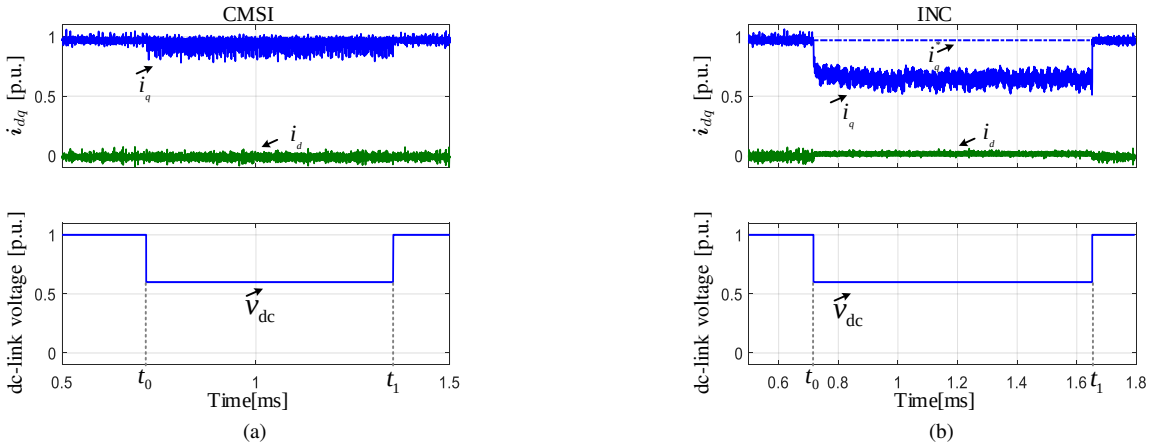

Fig. 16. The robustness comparisons between the CMSI and INC methods when the dc-link voltage drops from its rated to 60% value at t_0, then recovers to 100% value at t_1.

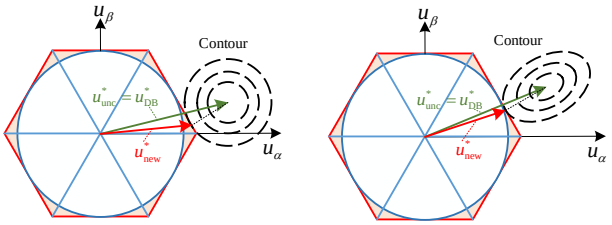

Fig. 17. Level sets of cost function J from problem (17). (**a**) Circular level sets. (**b**) Ellipsoidal level sets.

solver could be adopted to account for this. This part is under investigation and will be presented in a future work.

V. Discussion

It is clear that the optimal solution $\boldsymbol{u}^*_{\text{new}}$ of the QP-based DB problem is the same as the solutions in Sections III-A, III-B and III-C. However, this holds true only for symmetrical systems, like SPMSM drive systems. The reason is that the Hessian matrix $\boldsymbol{H}$ in (21) is diagonal and all its nonzero (i.e., diagonal) entries are equal. This means that the cost function J has circular level sets, see Fig. 17(a).

On the other hand, if machines with saliency are of interest, e.g., interior PMSMs (IPMSMs), then the diagonal entries of $\boldsymbol{H}$ are not equal. This gives rise to ellipsoidal level sets of J, as depicted in Fig. 17(b). As a result, the solution of the QP-based DB method is not the same as that of the other discussed methods presented in Sections III-A, III-B and III-C. It is worth mentioning that in such a case the modulating signals from Sections III-A, III-B and III-C are suboptimal, meaning that only the QP-based DB overmodulation method can provide the optimal modulating signal, and thus achieve the best possible performance. Further discussion of machines with saliency, however, is out of the scope of this paper.

VI. Conclusion

Considering the demand for maximum torque and power utilization of SPMSM systems, two efficient overmodulation methods are introduced in this paper. One of them is based on common-mode-saturation injection, which is very easy to implement on a real-world setting. Moreover, a constrained DB scheme is developed that adopts a PASM-based algorithm to find the optimal modulating signal. As shown, first in theory and then with the experiments conducted based on an SPMSM drive, the proposed methods are equivalent and achieve the same performance as the conventional overmodulation technique which is used in conjunction with SVM. Based on the presented analysis, it can be concluded that the proposed CMSI method is superior when SPMSM drives are of concern. On the other hand, the QP-based DB approach can be favorable when drives with saliency are of interest. This is the subject of a follow-up work.

Appendix A
Equivalence of SVM and CMSI Modulating Signals

Here the proof that $\boldsymbol{u}^*_{\text{new,CMSI}}$ is equal to $\boldsymbol{u}^*_{\text{new,SVM}}$ is provided.

Proof: Take the cases shown in Fig. 18 as an example, where points A and B correspond to the three-phase switch positions in the $\alpha\beta$ plane $\boldsymbol{S}_1 = [1\ -1\ -1]^T$ and $\boldsymbol{S}_2 = [1\ 1\ -1]^T$, respectively. More specifically, by mapping the three-phase switch positions $\boldsymbol{S}_1$ and $\boldsymbol{S}_2$ into the stationary $\alpha\beta$ plane via the Clarke transformation $\boldsymbol{K}$, it follows that $A = [\frac{4}{3}\ 0]^T$, $B = [\frac{2}{3}\ \frac{2\sqrt{3}}{3}]^T$ and $\overrightarrow{AB} = [-\frac{2}{3}\ \frac{2\sqrt{3}}{3}]^T$.

Consider the unconstrained modulating signal on the $\alpha\beta$ plane

$$C = \boldsymbol{u}^*_{\text{unc}} = [\alpha\ \beta]^T, \tag{27}$$

with

$$\alpha \geq \sqrt{3}\beta, \quad \beta \geq 0 \tag{28a}$$

$$3\alpha + \sqrt{3}\beta > 4, \tag{28b}$$

where (28a) indicates that $\arctan(\frac{\beta}{\alpha}) \in [0,\ \frac{\pi}{3}]$, and (28b) indicates that C is beyond the boundary of the voltage hexagon. Mapping $\boldsymbol{u}^*_{\text{unc}}$ into the three-phase abc plane via the inverse Clarke transformation yields

$$\boldsymbol{u}_{abc,\text{unc}} = \boldsymbol{K}^{-1}\boldsymbol{u}^*_{\text{unc}} = \begin{bmatrix} 1 & 0 \\ -\frac{1}{2} & \frac{\sqrt{3}}{2} \\ -\frac{1}{2} & -\frac{\sqrt{3}}{2} \end{bmatrix} \begin{bmatrix} \alpha \\ \beta \end{bmatrix} = \begin{bmatrix} \alpha \\ -\frac{1}{2}\alpha + \frac{\sqrt{3}}{2}\beta \\ -\frac{1}{2}\alpha - \frac{\sqrt{3}}{2}\beta \end{bmatrix}. \tag{29}$$

By combining (28a) and (29), it follows that

$$\max(\boldsymbol{u}_{abc,\text{unc}}) = \alpha, \quad \min(\boldsymbol{u}_{abc,\text{unc}}) = -\frac{1}{2}\alpha - \frac{\sqrt{}}{}$$

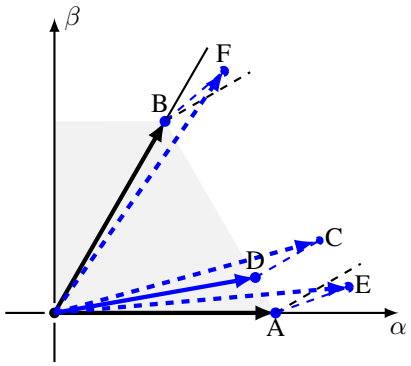

Fig. 18. Two-level inverter voltage vectors in the stationary ($\alpha\beta$) plane.

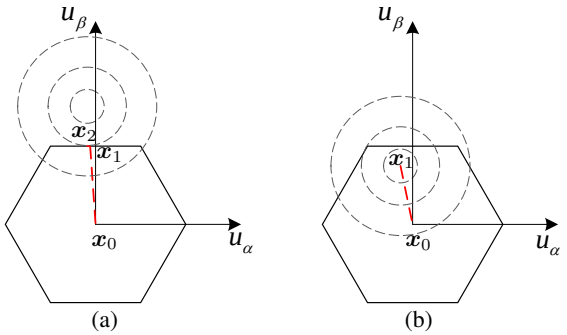

Fig. 19. Two examples of problem (21). (a) Constrained problem (see Example 1). (b) Unconstrained problem (see Example 2).

Therefore, after injecting the min/max common voltage

$$\begin{aligned} u_0 &= -\frac{1}{2}[\max(\boldsymbol{u}_{abc,\text{unc}}) + \min(\boldsymbol{u}_{abc,\text{unc}})] \\ &= -\frac{1}{4}\alpha + \frac{\sqrt{3}}{4}\beta\,, \end{aligned} \tag{31}$$

the modulating signal becomes

$$\boldsymbol{u}_{abc,\text{com}} = \boldsymbol{u}_{abc,\text{unc}} + u_0 = \begin{bmatrix} \frac{3}{4}\alpha + \frac{\sqrt{3}}{4}\beta \\ -\frac{3}{4}\alpha + \frac{3\sqrt{3}}{4}\beta \\ -\frac{3}{4}\alpha - \frac{\sqrt{3}}{4}\beta \end{bmatrix}. \tag{32}$$

Then, according to (28b), we know that $\frac{3}{4}\alpha + \frac{\sqrt{3}}{4}\beta > 1$ and $-\frac{3}{4}\alpha - \frac{\sqrt{3}}{4}\beta < -1$. This implies that

$$\begin{aligned} \text{sat}(\boldsymbol{u}_{abc,\text{com}}) &= \min(\max(\boldsymbol{u}_{abc,\text{com}}, \ -1), \ 1) \\ &= \begin{bmatrix} 1 \\ -\frac{3}{4}\alpha + \frac{3\sqrt{3}}{4}\beta \\ -1 \end{bmatrix}. \end{aligned} \tag{33}$$

Let D denote the new modulation signal $\boldsymbol{u}^*_{\text{new,CMSI}}$ in the stationary $\alpha\beta$ plane

$$\begin{aligned} D = \boldsymbol{K}\text{sat}(\boldsymbol{u}_{abc,\text{com}}) &= \frac{2}{3}\begin{bmatrix} 1 & -\frac{1}{2} & -\frac{1}{2} \\ 0 & \frac{\sqrt{3}}{2} & -\frac{\sqrt{3}}{2} \end{bmatrix}\begin{bmatrix} 1 \\ -\frac{3}{4}\alpha + \frac{3\sqrt{3}}{4}\beta \\ -1 \end{bmatrix} \\ &= \begin{bmatrix} 1 + \frac{\alpha}{4} - \frac{\sqrt{3}}{4}\beta \\ \frac{\sqrt{3}}{3} - \frac{\sqrt{3}}{4}\alpha + \frac{3}{4}\beta \end{bmatrix}, \end{aligned} \tag{34}$$

and

$$\overrightarrow{CD} = D - C = \begin{bmatrix} 1 - \frac{3\alpha}{4} - \frac{\sqrt{3}}{4}\beta \\ \frac{\sqrt{3}}{3} - \frac{\sqrt{3}}{4}\alpha - \frac{1}{4}\beta \end{bmatrix}. \tag{35}$$

From (35) it directly follows that

$$\overrightarrow{AB} \cdot \overrightarrow{CD} = [-\frac{2}{3} \ \ \frac{2\sqrt{3}}{3}]\begin{bmatrix} 1 - \frac{3\alpha}{4} - \frac{\sqrt{3}}{4}\beta \\ \frac{\sqrt{3}}{3} - \frac{\sqrt{3}}{4}\alpha - \frac{1}{4}\beta \end{bmatrix} = 0\,. \tag{36}$$

Therefore, it can be concluded that $\overrightarrow{AB} \perp \overrightarrow{CD}$, implying that $\boldsymbol{u}^*_{\text{new,CMSI}}$ is equal to $\boldsymbol{u}^*_{\text{new,SVM}}$.

Note that we have assumed so far that the b-phase value of $\boldsymbol{u}_{abc,\text{com}}$ is between -1 and 1, i.e., $-1 \leq -\frac{3}{4}\alpha + \frac{3\sqrt{3}}{4}\beta \leq 1$. Point E in Fig. 18 shows an example of the unconstrained solution when $-\frac{3}{4}\alpha + \frac{3\sqrt{3}}{4}\beta \leq -1$. In such a case, and by following the same deduction, we can find that the new modulating signal after the min/max common-mode injection and saturation will be point A. Similarly, point F in Fig. 18 shows an example of the unconstrained solution when $-\frac{3}{4}\alpha + \frac{3\sqrt{3}}{4}\beta \geq 1$. The new modulating signal after the min/max common-mode injection and saturation will be point B. It is evident that among all the points in the voltage hexagon points A and B have the shortest distance to E and F, respectively. The same conclusion can be drawn for all points outside the voltage hexagon by simply following the aforementioned analysis.

Appendix B
Illustrative Examples of the QP Solver

To better understand the working principle of the discussed QP solver, the following examples are provided.

Example 1: Consider the problem shown in Fig. 19(a). There is an active inequality constraint in the solution process, in which

$$\boldsymbol{H} = \begin{bmatrix} 0.0536 & 0 \\ 0 & 0.0536 \end{bmatrix}, \boldsymbol{f} = \begin{bmatrix} 0.0066 \\ -0.0933 \end{bmatrix}. \tag{37}$$

The origin is considered as the initial point, i.e., $\boldsymbol{x}_0 = \boldsymbol{0}$. None of the constraints is active at the beginning of the process, thus $\boldsymbol{\mathcal{W}}_0 = \emptyset$. Solving (24) at the first iteration yields $\boldsymbol{p}_0 = [-0.1233 \quad 1.7421]^T$. Accordingly, (26) provides the step-length $\alpha_0 = 0.6628 < 1$, which is blocked by constraint $\boldsymbol{a}_2$, see Fig. 19(a).

In the next iteration of the solution process (i.e., $\kappa = 1$), the initial point is $\boldsymbol{x}_1 = \boldsymbol{x}_0 + \alpha_0\boldsymbol{p}_0 = [-0.0817 \quad 1.1547]^T$. Moreover, at this iteration the blocking constraint $\boldsymbol{a}_2$ is added to the working set, i.e., $\boldsymbol{\mathcal{W}}_1 = \{2\}$. With this information, solving (24) yields $\boldsymbol{p}_1 = [-0.0416 \quad 0]^T$, and the new step-length is 1. There are no blocking constraints at this step, hence the working set at this step remains the same, i.e., $\boldsymbol{\mathcal{W}}_2 = \{2\}$.

At the next iteration ($\kappa = 2$), the new initial point is $\boldsymbol{x}_2 = [-0.1233 \quad 1.1547]^T$, and solving (24) gives $\boldsymbol{p}_2 = \boldsymbol{0}$. As (25) yields a multiplier $\boldsymbol{\lambda}_2 = \{0.0315\} > \boldsymbol{0}$, it indicates that the solution has been found.[3] Hence, $\boldsymbol{u}^*_{\text{qp}} = \boldsymbol{x}_2$ and the process terminates.

Example 2: As a second example, consider the case where all the constraints are inactive, as illustrated in Fig. 19(b), in which

$$\boldsymbol{H} = \begin{bmatrix} 0.0536 & 0 \\ 0 & 0.0536 \end{bmatrix}, \boldsymbol{f} = \begin{bmatrix} 0.0096 \\ -0.0462 \end{bmatrix}. \tag{38}$$

In a similar fashion, the solution process starts with $\boldsymbol{x}_0 = \boldsymbol{0}$ and $\boldsymbol{\mathcal{W}}_0 = \emptyset$. By solving the unconstrained problem, the solution of (24) is $\boldsymbol{p}_0 = [-0.1793 \quad 0.8629]^T$. The step-length formula (26) yields $\alpha_0 = 1$. The new iteration starts with $\boldsymbol{x}_1 = [-0.1793 \quad 0.8629]^T$, and $\boldsymbol{\mathcal{W}}_1 = \boldsymbol{\mathcal{W}}_0$. By solving the unconstrained problem (as no constraints are active),

[3]The subscript of $\boldsymbol{\lambda}_2$ refers to the iteration.

$\boldsymbol{p}_1 = \mathbf{0}$ and $\boldsymbol{\lambda}_1 = \{0\}$ are obtained. As the Lagrangian multiplier is zero, the solution is set as $\boldsymbol{u}^*_{\mathrm{qp}} = \boldsymbol{x}_1$ and the algorithm terminates. Finally, it is worth mentioning that since the problem in this example is unconstrained, the optimal modulating signal $\boldsymbol{u}^*_{\mathrm{qp}}$ is the same as $\boldsymbol{u}^*_{\mathrm{DB}}$ in (8).

REFERENCES

[1] M. C. Chou, C. M. Liaw, S. B. Chien, F. H. Shieh, J. R. Tsai, and H. C. Chang, "Robust current and torque controls for PMSM driven satellite reaction wheel," *IEEE Transactions on Aerospace and Electronic Systems*, vol. 47, no. 1, pp. 58–74, 2011.

[2] S. Silber, J. Sloupensky, P. Dirnberger, M. Moravec, W. Amrhein, and M. Reisinger, "High-speed drive for textile rotor spinning applications," *IEEE Transactions on Industrial Electronics*, vol. 61, no. 6, pp. 2990–2997, 2014.

[3] Z. Ping, T. Wang, Y. Huang, H. Wang, J.-G. Lu, and Y. Li, "Internal model control of PMSM position servo system: Theory and experimental results," *IEEE Transactions on Industrial Informatics*, vol. 16, no. 4, pp. 2202–2211, 2020.

[4] W. Su, H. Eichi, W. Zeng, and M.-Y. Chow, "A survey on the electrification of transportation in a smart grid environment," *IEEE Transactions on Industrial Informatics*, vol. 8, no. 1, pp. 1–10, 2012.

[5] R. Gabriel, W. Leonhard, and C. J. Nordby, "Field-Oriented control of a standard AC motor using microprocessors," *IEEE Transactions on Industry Applications*, vol. IA-16, no. 2, pp. 186–192, 1980.

[6] H. S. Black, *Modulation theory*. van Nostrand, 1953.

[7] T. Geyer, *Model predictive control of high power converters and industrial drives*. John Wiley & Sons, 2016.

[8] A. Brosch, O. Wallscheid, and J. Böcker, "Model predictive control of permanent magnet synchronous motors in the overmodulation region including six-step operation," *IEEE Open Journal of Industry Applications*, vol. 2, pp. 47–63, 2021.

[9] S. Bolognani and M. Zigliotto, "Space vector fourier analysis of svm inverters in the overmodulation range," in *Proceedings of International Conference on Power Electronics, Drives and Energy Systems for Industrial Growth*, vol. 1, 1996, pp. 319–324 vol.1.

[10] Y.-C. Kwon, S. Kim, and S.-K. Sul, "Six-step operation of PMSM with instantaneous current control," *IEEE Transactions on Industry Applications*, vol. 50, no. 4, pp. 2614–2625, 2014.

[11] P. Karamanakos, E. Liegmann, T. Geyer, and R. Kennel, "Model predictive control of power electronic systems: Methods, results, and challenges," *IEEE Open Journal of Industry Applications*, vol. 1, pp. 95–114, 2020.

[12] P. Karamanakos, T. Geyer, and S. Manias, "Direct voltage control of dc–dc boost converters using enumeration-based model predictive control," *IEEE Transactions on Power Electronics*, vol. 29, no. 2, pp. 968–978, 2014.

[13] F. Morel, X. Lin-Shi, J.-M. Retif, B. Allard, and C. Buttay, "A comparative study of predictive current control schemes for a permanent-magnet synchronous machine drive," *IEEE Transactions on Industrial Electronics*, vol. 56, no. 7, pp. 2715–2728, 2009.

[14] M. Preindl and S. Bolognani, "Model predictive direct torque control with finite control set for PMSM drive systems, part 2: Field weakening operation," *IEEE Transactions on Industrial Informatics*, vol. 9, no. 2, pp. 648–657, 2013.

[15] J. Holtz, "Advanced PWM and predictive control—An overview," *IEEE Transactions on Industrial Electronics*, vol. 63, no. 6, pp. 3837–3844, 2016.

[16] P. Karamanakos and T. Geyer, "Guidelines for the design of finite control set model predictive controllers," *IEEE Transactions on Power Electronics*, vol. 35, no. 7, pp. 7434–7450, 2020.

[17] A. A. Ahmed, B. K. Koh, and Y. I. Lee, "A comparison of finite control set and continuous control set model predictive control schemes for speed control of induction motors," *IEEE Transactions on Industrial Informatics*, vol. 14, no. 4, pp. 1334–1346, 2018.

[18] Q. Yang, P. Karamanakos, W. Tian, X. Gao, X. Li, T. Geyer, and R. Kennel, "Computationally efficient fixed switching frequency direct model predictive control," *IEEE Transactions on Power Electronics*, vol. 37, no. 3, pp. 2761–2777, 2021.

[19] G. Cimini, D. Bernardini, S. Levijoki, and A. Bemporad, "Embedded model predictive control with certified real-time optimization for synchronous motors," *IEEE Transactions on Control Systems Technology*, vol. 29, no. 2, pp. 893–900, 2021.

[20] Z. Yan and J. Wang, "Model predictive control of nonlinear systems with unmodeled dynamics based on feedforward and recurrent neural networks," *IEEE Transactions on Industrial Informatics*, vol. 8, no. 4, pp. 746–756, 2012.

[21] H.-T. Moon, H.-S. Kim, and M.-J. Youn, "A discrete-time predictive current control for PMSM," *IEEE Transactions on Power Electronics*, vol. 18, no. 1, pp. 464–472, 2003.

[22] W. Tian, Q. Yang, X. Li, X. Gao, X. Chen, and R. Kennel, "Deadbeat control for AC drive systems with optimal dynamic performance," in *2020 IEEE Energy Conversion Congress and Exposition (ECCE)*, 2020, pp. 5777–5783.

[23] J.-K. Seok, J.-S. Kim, and S.-K. Sul, "Overmodulation strategy for high-performance torque control," *IEEE Transactions on Power Electronics*, vol. 13, no. 4, pp. 786–792, 1998.

[24] A. Sarajian, C. F. Garcia, Q. Guan, P. Wheeler, D. A. Khaburi, R. Kennel, J. Rodriguez, and M. Abdelrahem, "Overmodulation methods for modulated model predictive control and space vector modulation," *IEEE Transactions on Power Electronics*, vol. 36, no. 4, pp. 4549–4559, 2021.

[25] C. F. Garcia, C. A. Silva, J. R. Rodriguez, P. Zanchetta, and S. A. Odhano, "Modulated model-predictive control with optimized overmodulation," *IEEE Journal of Emerging and Selected Topics in Power Electronics*, vol. 7, no. 1, pp. 404–413, 2018.

[26] B. McGrath, D. Holmes, and T. Lipo, "Optimized space vector switching sequences for multilevel inverters," *IEEE Transactions on Power Electronics*, vol. 18, no. 6, pp. 1293–1301, 2003.

[27] J. Nocedal and S. Wright, *Numerical optimization*. Springer Science & Business Media, 2006.

Qianwen Duan was born in Xi'an, Shaanxi, China, in 1994. She received the B.S. degree in automation from Xi'an University of Post & Telecommunications in 2016, and the Ph.D. degree in signal and information processing from the University of Chinese Academy of Sciences, in 2022, respectively.

Currently, she is a postdoctoral fellow in optical engineering with the Institute of Optics and Electronics, Chinese Academy of Sciences. Her research interests include set-point tracking control, image-based serving control, and predictive control.

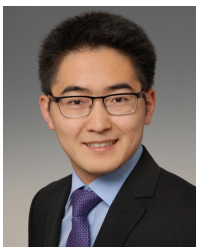

Wei Tian was born in Taizhou, Jiangsu, China, in 1989. He received the B.Eng. degree in electrical engineering and automation from Central South University (CSU), Changsha, China, in 2012 and the M.Sc. degree in electrical power engineering from RWTH Aachen University, Aachen, Germany, in 2015.

Since 2016, he has been pursuing the Ph.D. degree at the Chair of Electrical Drive Systems and Power Electronics, and the Chair of High-Power Converter Systems, Technical University of Munich (TUM), Munich, Germany.

His research interests include power electronics and electrical drives, model predictive control, and modular multilevel converter.

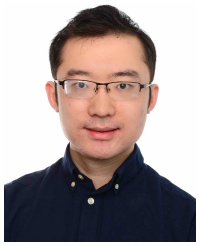

Qifan Yang was born in Anhui, China, in 1995. He received the B.Eng. degree in electrical engineering Xi'an Jiaotong University, Xi'an, Shaanxi, China, in 2016, and the M.S. degree in electrical power engineering from Technical University of Munich, Munich, Germany, in 2019. Since 2019, he has been pursuing the Ph.D. degree at the Chair of Electrical Drive Systems and Power Electronics, Technical University of Munich (TUM), Germany.

His research interests include optimal control, power electronics and electrical drives.

Xiaonan Gao (S'18-M'21) was born in Liaoning, China, in 1990. He received the B.S. and M.S. degrees in electrical engineering from the Dalian University of Technology (DUT), Dalian, China, in 2013 and 2016, respectively.

Since 2016, he has been pursuing the Ph.D. degree at the Chair of Electrical Drive Systems and Power Electronics, Technical University of Munich (TUM), Germany. His research interests include power electronics and electrical drives, predictive control, and multilevel converters.

Yao Mao was born in Chongqing, China, in 1978. He received the B.S. degree in automation from Chongqing University, and the Ph.D. degree in signal processing from the Institute of Optics and Electronics, Chinese Academy of Sciences, in 2001, 2012, respectively.

Since 2001, he has worked on electro-optical tracking control with the Institute of Optics and Electronics, Chinese Academy of Sciences, Chengdu, China, where he is currently a full professor and received the Distinguished Scientific Achievement Award in 2011. He has authored and coauthored more than 50 internationally refereed papers. His main research interests include machine learning, predictive filtering and electro-optical tracking system control.

Petros Karamanakos (S'10 – M'14 – SM'19) received the Diploma and Ph.D. degrees in electrical and computer engineering from the National Technical University of Athens (NTUA), Athens, Greece, in 2007, and 2013, respectively.

From 2010 to 2011 he was with the ABB Corporate Research Center, Baden-Dättwil, Switzerland, where he worked on model predictive control strategies for medium-voltage drives. From 2013 to 2016 he was a PostDoc Research Associate in the Chair of Electrical Drive Systems and Power Electronics, Technische Universität München, Munich, Germany. Since 2016, he has been with the Faculty of Information Technology and Communication Sciences, Tampere University, Tampere, Finland, where he is currently an Associate Professor. His main research interests lie at the intersection of optimal control, mathematical programming and power electronics, including model predictive control and optimal modulation for power electronic converters and ac variable speed drives.

Dr. Karamanakos received the 2014 Third Best Paper Award of the IEEE Transactions on Industry Applications and two Prize Paper Awards at conferences. He serves as an Associate Editor of the IEEE Transactions on Industry Applications and of the IEEE Open Journal of Industry Applications. He is a Regional Distinguished Lecturer of the IEEE Power Electronics Society in the years 2022 and 2023.

Ralph Kennel (M'88-SM'96) was born in Kaiserslautern, Germany, in 1955. He received the Diploma and Dr. Ing. (Ph.D.) degrees in electrical engineering from University of Kaiserslautern, Kaiserslautern, Germany, in 1979 and 1984, respectively.

From 1983 to 1999, he worked on several positions with Robert BOSCH GmbH, Gerlingen, Germany. Until 1997, he was responsible for the development of servo drives. From 1994 to 1999, he was a Visiting Professor with the University of Newcastleupon-Tyne, Newcastle-upon-Tyne, U.K. From 1999 to 2008, he was a Professor of electrical machines and drives with Wuppertal University, Wuppertal, Germany. Since 2008, he has been the head of the Chair of electrical drive systems and power electronics at Technical University of Munich, Munich, Germany. His current main interests include renewable energy systems, sensorless control of ac drives, predictive control of power electronics, and hardware-in-the-loop systems.

Dr. Kennel is a Chartered Engineer in the U.K., within IEEE, he is a Treasurer of the Germany Section as well as ECCE Global Partnership Chair of the Power Electronics society. He is currently an Associate Editor for IEEE Transactions on Power Electronics.

Marcelo Lobo Heldwein (S'99-M'08-SM'13) received the B.S. and M.S. degrees in electrical engineering from the Federal University of Santa Catarina (UFSC), Florianópolis, Brazil, in 1997 and 1999, respectively, and his Ph.D. degree from the Swiss Federal Institute of Technology (ETH Zurich), Zurich, Switzerland, in 2007.

He is currently the head of the Chair of High-Power Converter Systems with the Department of Energy and Process Engineering at the Technical University of Munich (TUM), Munich, Germany.

From 1999 to 2003, he worked with industry, including R&D activities at the Power Electronics Institute, Brazil and Emerson Network Power, in Brazil and Sweden. He was a Postdoctoral Fellow at the ETH Zurich and at the UFSC from 2007 to 2009. From 2010 to 2022 he was a Professor with the Department of Electronics and Electrical Engineering at the UFSC. Dr. Heldwein is a member of the Brazilian Power Electronic Society (SOBRAEP) and a member of the Advisory Board of PCIM Europe.

His research interests include Power Electronics, Advanced Power Distribution Technologies and Electromagnetic Compatibility.